Nanoscale

PAPER

View Article Online
View Journal

Cite this: DOI: 10.1039/d5nr04648c

Compositional control of the effective magnetic anisotropy in Mn and Co substituted spinel nanoparticles

Alexander Malaj,[a] Cathryn Leies,[a] Zachary Caprow,[a] Venkata Rohit Punyapu,[b] Ehimen A. Odion,[c] Rachel Getman,[b] Karen L. Livesey,[d] Suvra S. Laha*[a] and O. Thompson Mefford *[a,c]

Received 3rd November 2025,
Accepted 28th April 2026

DOI: 10.1039/d5nr04648c

rsc.li/nanoscale

It has been shown through density functional theory (DFT) calculations that the magnetocrystalline anisotropy (MAE) for iron-based spinel nanoparticles can be altered through the addition of varying amounts of transition metals into their spinel structures. In this work, seven monodisperse spherical nanoparticle series were synthesized with varying amounts of Fe, Mn, and Co to target specific effective anisotropy (K_{eff}) values that were calculated using DFT, giving the formula: $Fe_{3-x-y}Mn_xCo_yO_4$. The K_{eff} values determined from DC magnetometry ranged from 46–128 kJ m^{-3}, increasing upon the addition of Mn, and increasing upon the addition of Co, verifying the trend that the DFT simulations predicted. The K_{eff} value determined from DC magnetometry was lower than that predicted by DFT for the spinel nanoparticles with high cobalt substitution, and comparable for the other samples. From the AC susceptibility data, the trend in the anisotropy strength amongst the series of seven particles matched that extracted from the DC magnetometry data. Through these findings, it is shown that K_{eff} is tunable by altering cationic ratios in spinel nanoparticles.

1 Introduction

Magnetic nanoparticles are capable of dissipating heat when exposed to an alternating magnetic field.[1] The heating efficiency of these particles is measured using specific absorption rate (SAR), which outlines the amount of heat energy released by a mass of nanoparticles over time, and is given by[2]

$$\mathrm{SAR} = C\frac{m_s}{m_p}\frac{\mathrm{d}T}{\mathrm{d}t}, \quad (1)$$

where C is the specific heat of the dispersant, m_s is the mass of the dispersing fluid, m_p is the mass of the magnetic material in the nanoparticles, T is temperature, and t is time.

A sufficiently small nanoparticle (*i.e.*, diameter less than 100 nm) will exhibit a single magnetic domain, which is usually considered to contain two stable orientations which are antiparallel to each other, along the so-called easy axis.[3] The energy required to flip the nanoparticle's moment between the two orientations is proportional to the particle's magnetic volume (V_C) and the effective magnetic anisotropy energy density (K_{eff}), which includes anisotropy factors such as: magnetocrystalline anisotropy, shape anisotropy, and particle interaction anisotropy.[4] It is important to note that this effective uniaxial anisotropy assumption is used as a simplification for modeling.[5] Realistically, the intrinsic magnetocrystalline anisotropy of most spinel nanoparticles is cubic.[6–8] Upon reaching a high enough thermal energy (k_BT), where k_B is the Boltzmann constant, the particles will continuously flip their magnetic moments between the two directions along the easy axis, yielding an average magnetic moment very close to zero.[4] This phenomenon is known as superparamagnetism. The mean time between two flips along the easy axis is known as the Néel relaxation time, which stems from the Néel–Arrhenius formula and is given by

$$\tau_N = \tau_0 \exp\left[\frac{K_{eff}V_C}{k_BT}\right], \quad (2)$$

where τ_0 is an attempt time parameter between 10^{-13} and 10^{-9} s,[9] K_{eff} is the effective anisotropy energy density, V_C is the volume of the magnetic core, k_B is the Boltzmann constant, and T is temperature. It should be noted that nanoparticles also experience a Brownian relaxation time – they physically rotate – which depends on the hydrodynamic radius of the

[a]Department of Materials Science and Engineering, Clemson University, Clemson, SC 29634, USA. E-mail: slaha@clemson.edu, mefford@clemson.edu
[b]William G. Lowrie Department of Chemical and Biomolecular Engineering, The Ohio State University, Columbus, OH 43210, USA
[c]Department of Chemistry, Clemson University, Clemson, SC 29634, USA
[d]School of Information and Physical Sciences, University of Newcastle, University Drive, Callaghan, 2308 NSW, Australia

nanoparticles and the viscosity of the media they are suspended in. In highly viscous media, such as cell tissue, Néel relaxation is usually much quicker and will dominate the particle's overall relaxation time.[4] The amount of heat that magnetic nanoparticles generate is dependent on the strength and frequency of the alternating magnetic field.[10]

Efforts have been made to tune the Néel relaxation time of nanoparticles by manipulating their core sizes, shapes, and elemental compositions.[11] Manipulating the elemental composition includes doping spinel nanoparticles with one metallic species such as: zinc, cobalt, manganese, silver, and gold.[11] Catalytic activity, and the performance of these magnetic nanoparticles is highly dependent on their composition, morphology, and dimensions.[11] Specifically, tuning the K_{eff} and M_s of superparamagnetic nanoparticles is highly sought after, as the optimal values for these properties will change depending on their application.

Recently, computational density functional theory (DFT) models were used by some of us to explore what effect cationic substitutions have on the M_s and anisotropy energy for various spinel compositions.[12] Briefly, a ferrite model was used based on the calculated bulk unit cell of magnetite (Fe_3O_4). Eight repeats of the magnetite formula unit ($Fe_{24}O_{32}$) were used to allow for many different ion substitutions. Among these bi-cationic and tri-cationic substitutions, M_s, magnetocrystalline anisotropy energy, and crystal structure were simulated. The model is based on the spinel structure with the space group $Fd\bar{3}m$, which has a cubic crystal symmetry. K_{eff} was calculated as the energy density required to reorient the magnetic moment within a crystal from the "easy" axis to the "hard" axis. The [0,0,1], [1,0,0], and [0,1,0] crystallographic directions were evaluated this way, as the calculations for the [0,1,1], [1,0,1], [1,1,0] and [1,1,1] directions resulted in electronic energies that were significantly more positive, suggesting they were less reliable for large-scale DFT calculations. Of the [0,0,1], [1,0,0], and [0,1,0] directions, the direction that was calculated to have the lowest electronic energy was the easy axis, and the direction that was calculated to have the highest electronic energy was the hard axis. These hard and easy axes were subtracted from each other to give the magnetocrystalline anisotropy energy density (MAE). To calculate the M_s of the spinel nanoparticles, the total number of unpaired electronic in the unit cell is multiplied by the Bohr magneton (μ_B) and divided by the unit cell's volume. While these calculations are useful as a qualitative guidance, some of the limitations of DFT should be stated, such as the energy differences between cation configurations not being representative of the experimental distribution of Fe, Mn, and Co across the spinel structure.[13] DFT also assumes idealized crystals that lack the structural heterogeneities that are found in real crystals and is also conducted at absolute zero, causing the theoretical calculations to deviate from experiment.[14] Following this guidance, the optimal saturation magnetization and magnetocrystalline anisotropy energy density combination of values calculated in that work is plotted in Fig. 1 (solid line) based on the work of Carrey *et al.*,[15] for a magnetic field strength of 20 kA m^{-1} and a frequency of 205 kHz. The black dots represent different stoichiometric compositions of Fe, Mn, and Co, and their corresponding M_s and MAE values, adapted from ref. 12.

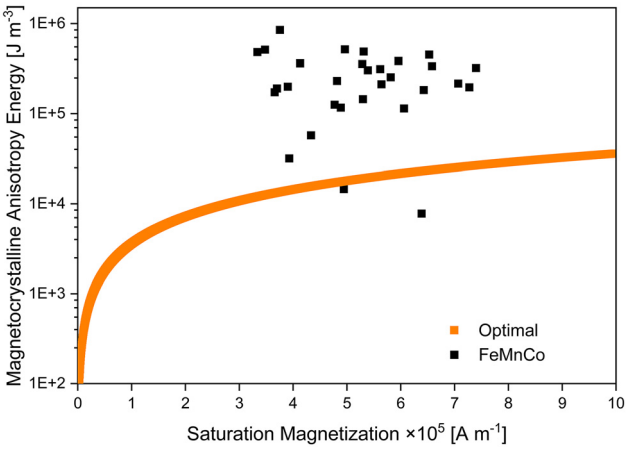

Fig. 1 Optimal MAE and saturation magnetization combination of values (solid line) predicted at a magnetic field strength of 20 kA m^{-1} and a frequency of 205 kHz.[15] The dots correspond to the M_s and MAE values of spinels with different stoichiometric compositions of Fe, Mn, and Co, calculated in ref. 12.

Mono or bi-cationic nanoparticles have been shown to have limited tunability of K_{eff} through influencing oxidation state, site occupancy, exchange pathways, and spin–orbit coupling.[16] For example, Co substitution has been shown to enhance magnetocrystalline anisotropy through spin–orbit coupling but often reduces the overall M_s of the nanoparticle.[17] Mn substitution often reduces magnetocrystalline anisotropy.[18] Therefore, in bi-cationic nanoparticles, these changes in K_{eff}, M_s, and relaxation dynamics are strongly dependent on one another, constraining the tunability of the nanoparticles.[19] In contrast, multi-cationic species have been shown to provide broader control over K_{eff}, coercivity, and M_s as the introduction of a third cation adds a new degree of freedom that mono or bi-cationic nanoparticles cannot access, allowing nanoparticles with highly precise magnetic states to be synthesized.[20]

Recently, $Mn_xZn_{1-x}Fe_2O_4$ (x = 0–1) spherical superparamagnetic particles were synthesized using a triethylene glycol mediated solvothermal method.[21] At room temperature, these substitutions showed varying lower M_s values compared to magnetite, but reversed trends at 10 K.[21] $Zn_{0.5-x}Ca_xMg_{0.5}Fe_2O_4$ (x = 0.1 and 0.2) nanoparticles have also been synthesized for the purposes of controlled heating in magnetic hyperthermia, as the magnetic moment and heating efficiency of the nanoparticles can be adjusted by altering the calcium-to-zinc ratios.[22] The nanoparticles were experimentally determined to be biocompatible through analyzing cytotoxic effects on mouse muscle fibroblast and human breast cancer cell lines, showing a cell viability above 85% when hyperthermia treatment was not applied. Despite the potential for multi-cationic nanoparticles, experimental studies that correlate composition with K_{eff}, relaxation dynamics, and SAR remain scarce.

This work introduces seven nanoparticle series with varying cationic compositions giving the formula $Fe_{3-x-y}Mn_xCo_yO_4$, which were synthesized with targeted compositions based on the tertiary diagrams created from density functional theory (DFT) calculations.[12] The five nanoparticle points at the bottom of the tertiary diagram were chosen due to their predicted MAE and M_s values aligning with the point closest to the optimal curve in Fig. 1, which would theoretically cause them to dissipate the highest amount of energy per AC field cycle at a magnetic field strength of 20 kA m^{-1} and a frequency of 205 kHz. As the points read from left to right, incremental increases in Fe substitutions and incremental decreases in Mn substitutions occur, which are intended to span a controlled range of cationic substitutions. The points in the middle and top right of the tertiary diagram were targeted due to their higher MAE (K_{eff}) values upon a higher Co substitution, as shown in Fig. 2. The nanoparticles were synthesized using metal acetylacetonate precursors with a Mn oleate drip through a thermal decomposition route, based off of the extended Lamer drip synthesis method,[23,24] in an attempt to create monodisperse, spherical nanoparticles with similar diameters throughout the various cationic compositions to minimize the contributions of particle volume and shape to the anisotropy energy density K_{eff}. The nanoparticles' diameters were determined using high-resolution transmission electron microscopy (HR-TEM) and ImageJ software, and were found to be monodisperse, and ranged from 8.4–10.6 nm in diameter throughout each series. DC and AC magnetometry revealed an increase in K_{eff} upon increasing Mn content, and a high increase in K_{eff} upon increasing Co content. AC and calorimetric SAR experiments at a magnetic field strength of 20 kA m^{-1} and a magnetic field frequency of approximately 200 kHz revealed poor heating of each multi-cationic series, except for the high anisotropy, high cobalt substituted spinel nanoparticles (MM-2), which displayed an AC SAR value of 83 W g^{-1} and a calorimetric SAR value of 26.9 W g^{-1}. Section 2 outlines the synthesis methods guided by DFT, and the characterization methods. Results are presented in Section 3 including detailed analysis of the magnetometry data. Conclusions and outlook are presented in Section 4. This work guides future engineering of magnetic nanoparticles with tailored properties for applications like hyperthermia treatment.

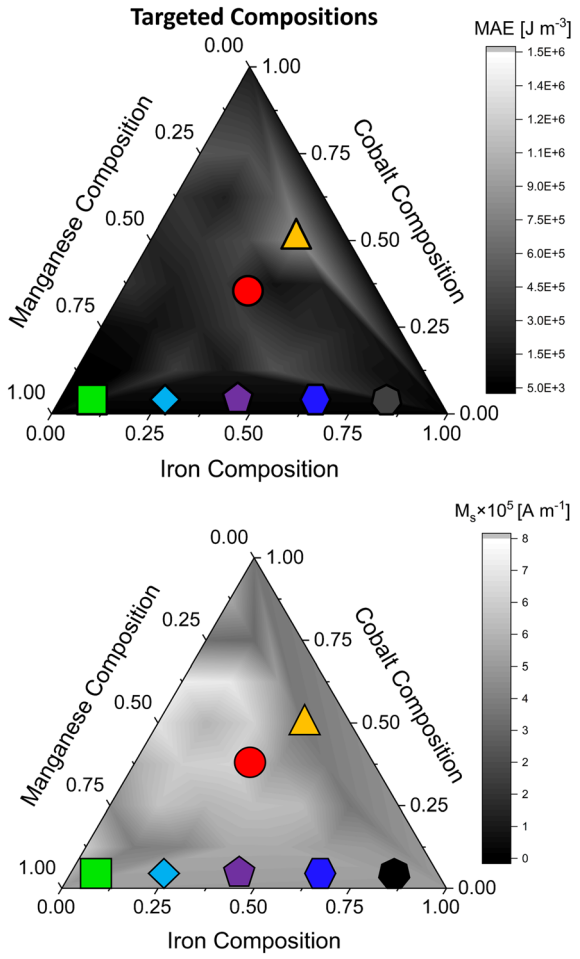

Sample	Fe Ion	Mn Ion	Co Ion	Fe Acac	Mn Oleate	Co Acac
MM-1	0.33	0.33	0.33	0.661	0.182	0.068
MM-2	0.35	0.1	0.55	0.664	0.020	0.113
MM-3	0.05	0.9	0.05	0.579	0.182	0.010
MM-4	0.25	0.7	0.05	0.635	0.142	0.010
MM-5	0.45	0.5	0.05	0.692	0.101	0.010
MM-6	0.65	0.30	0.05	0.748	0.061	0.010
MM-7	0.85	0.10	0.05	0.805	0.020	0.010

Fig. 2 Tertiary diagrams depicting DFT[12] targeted cationic compositions, the reagent weights in grams used in the synthesis and their corresponding magnetocrystalline anisotropy energies, and magnetic saturations.

2 Experimental

2.1 Synthesis of $Fe_{3-x-y}Mn_xCo_yO_4$ spinel nanoparticles

As shown in Fig. 2, five compositions along the bottom of the tertiary diagram were synthesized (MM-3 to MM-7), targeting lower MAE (K_{eff}) values. Additional compositions were synthesized at the middle of the diagram (MM-1) and at the region of high MAE (MM-2). Their corresponding targeted cationic compositions and precursor masses are also shown. The tertiary diagram on the right of Fig. 2 depicts the actual cationic compositions of each sample, which were slightly different from those targeted. Fig. 3 depicts the seven compositions again, with their predicted DFT M_s values shown by the gray scale (see scale bar). The samples were synthesized using a thermal decomposition drip method, adapted from the extended LaMer drip synthesis.[23] In a typical synthesis, iron and cobalt acetylacetonates were added to a 3-neck round bottom flask with 3 mL of oleic acid, and 5 mL of octadecene. Three rubber septums were attached to each end of the flask and the mixture was vortexed and sonicated until homogeneous. Using a syringe needle attached to a Schlenk line, a vacuum pump was used to degas the liquids until bubbles stopped forming. Manganese oleate and 5 mL of octadecene were also mixed, sonicated, and degassed in the same manner. A metal bath was used to heat the 3-neck flask to

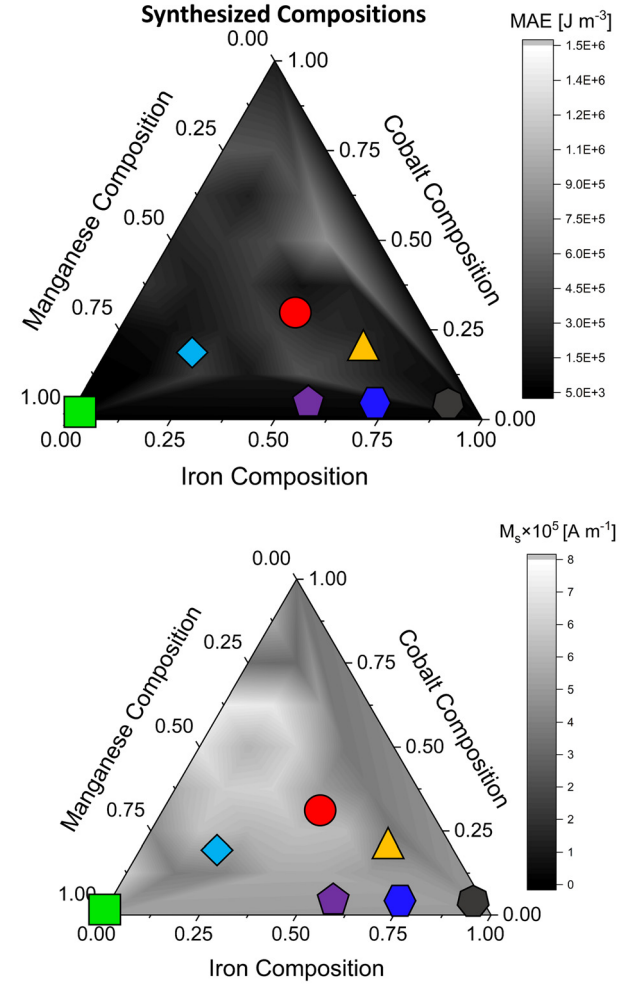

Tertiary Point	Target Composition	Actual Composition
MM-1	$Fe_{2.33}Mn_{0.33}Co_{0.33}$	$Fe_{2.40}Mn_{0.34}Co_{0.26}$
MM-2	$Fe_{2.35}Mn_{0.1}Co_{0.55}$	$Fe_{2.64}Mn_{0.24}Co_{0.13}$
MM-3	$Fe_{2.05}Mn_{0.9}Co_{0.05}$	$Fe_{1.77}Mn_{1.19}Co_{0.03}$
MM-4	$Fe_{2.25}Mn_{0.7}Co_{0.05}$	$Fe_{2.13}Mn_{0.63}Co_{0.23}$
MM-5	$Fe_{2.45}Mn_{0.5}Co_{0.05}$	$Fe_{2.57}Mn_{0.40}Co_{0.02}$
MM-6	$Fe_{2.65}Mn_{0.3}Co_{0.05}$	$Fe_{2.71}Mn_{0.26}Co_{0.02}$
MM-7	$Fe_{2.85}Mn_{0.1}Co_{0.05}$	$Fe_{2.89}Mn_{0.10}Co_{0.02}$

Fig. 3 Tertiary diagrams depicting synthesized cationic compositions, their corresponding magnetocrystalline anisotropy energies and their magnetic saturations predicted by DFT.[12] The compositions were verified through ICP-OES.

360 °C. The middle septum was removed to allow a mechanical stirrer with a glass stir rod to be inserted to stir the mixture at roughly 300 rpm. A syringe needle attached to a flowmeter was inserted through a rubber septum on the flask to allow house nitrogen to flow at 0.3 L min^{-1}. The manganese oleate solution was poured into a syringe and attached to a syringe pump. A long syringe needle was attached to the syringe and placed in the remaining septum to drip the precursor at 5 mL h^{-1}. The reaction was held at 360 °C for one hour and then removed to cool down to room temperature. Upon cooling, the nanoparticles were dispersed in two 50 mL centrifuge tubes by roughly halving the nanoparticle solution and adding 15 mL of hexane to each tube. 20 mL of methanol is then added to each tube, which are both centrifuged at 10 000 rpm for 3 minutes. Upon collecting some of the particles at the bottom of the tube, an oily layer remained at the top of the liquids. The dirty methanol was pipetted out, discarded, and fresh methanol was added again. The centrifuge tubes were shaken, sonicated, and centrifuged again. This process was repeated until the volume of the oily layer became minimal. The particles were then stored in hexane, parafilm wrapped, and placed in a refrigerator for storage.

2.2 Characterization techniques

2.2.1 TEM characterization. A Hitachi 7830 high resolution transmission electron microscope (HR-TEM) operating at 120 kV and 10 μA was used to obtain images of the nanoparticles. One droplet of the diluted nanoparticle mixture in hexane was dropped onto formvar/carbon on 200 mesh copper TEM grids purchased from Electron Microscopy Sciences. ImageJ software was used to measure the diameters of the particles through applying a threshold to the image to distinguish the particles from the background. A scale was applied, followed by the "analyze particles" function to automatically determine the Feret diameters of 300 nanoparticles. (300 nanoparticles are widely used as a sample size to provide sufficient statistical information for a nanoparticle series.[25]) An analysis of variance (ANOVA) with a significance level of $\alpha = 0.05$ was used to determine if any of the mean diameters statistically differed among the samples.

2.2.2 Analysis of cation content. A Thermo iCAP 7200 inductively coupled plasma optical emission spectroscopy (ICP-OES) analyzer equipped with Qtegra ISDS software was used to analyze the elemental compositions of each nanoparticle series.

2.2.3 DC magnetic characterization. A physical property measurement system (PPMS) by Quantum Design was used to obtain magnetization *versus* field (*M vs. H*) curves using a field strength of ±3 T at 300 K. The zero-field cooled (ZFC) and field-cooled (FC) curves were measured using a magnetic field strength of 10 mT or 100 Oe, and temperatures ranging from 2 K to 300 K.

2.2.4 AC magnetic characterization. The multi-cationic nanoparticles were dispersed into cotton balls which were then loaded into the PPMS using a cut plastic straw as a sample holder. The AC magnetic susceptibility (ACMS) II option was used to generate the magnetization response of the nanoparticles *versus* temperature (2 K–300 K; for MM-2, the temperature range extends to 350 K) in terms of real and imaginary susceptibility through varying the frequency of the AC magnetic field was varied from 100 Hz to 10 000 Hz. The experiments were conducted at a 10 Oe AC excitation field under zero DC bias conditions.

2.2.5 Calorimetric SAR. An Ambrell EasyHeat Induction Heating System was used to measure SAR calorimetrically. An alternating current at 205 kHz was applied through the instrument's coil containing 1 mL of a known concentration of

nanoparticles dispersed in toluene inside a non-magnetic holder. The surrounding custom 3D printed sample holder was kept at 27 °C through a temperature-controlled water bath from PolyScience. The temperature of the nanoparticle dispersion was measured with a Neoptix brand fiber optic cable and a Reflex temperature sensor recorder. The initial slopes of the resulting temperature *versus* time graphs were taken to calculate SAR values. This was repeated three times for each nanoparticle series, and the resulting average was taken to be the overall calorimetric SAR value. The calorimetric experiments were also repeated for a field strength of 12.7 kA m^{-1} and a field frequency of 376 kHz. The calorimetric experiments were also repeated for a field strength of 12.7 kA m^{-1} and a field frequency of 376 kHz to probe heating behavior at higher frequencies, with each nanoparticle series only having one repeat.

2.2.6 AC magnetometric SAR. AC magnetometry measurements of the nanoparticles were carried out on a 40 μL toluene magnetic suspension by commercial inductive magnetometers from Nanotech Solutions. Each magnetization cycle was obtained from three repetitions, resulting in the averaged magnetization cycle and the related magnetic parameters: coercive force H_c, remanent magnetization M_r, and loop area representative of magnetic losses. The magnetometric specific absorption rate (SAR) values were determined for the following expression $\mathrm{SAR} = \frac{f}{c}A$, by calculating the area of the resulting hysteresis loop, where A is the AC magnetic area, c is the nanoparticle elemental (cationic) weight concentration, and f is the AC magnetic field frequency.[10] Magnetization units were normalized by total cationic masses obtained by ICP-OES.

3 Results and discussion

3.1 Structural characterization

For each series, 300 nanoparticles were measured showing mean diameters near 10 nm. From Fig. 4, the lower Mn substituted spinel nanoparticles (MM-6 and MM-7) are slightly smaller at 8.8 and 8.4 nm, respectively. From MM-3 to MM-7, increasing Fe and decreasing Mn content generally correlates with decreasing nanoparticle diameters. MM-1 and MM-2, (which have higher cobalt content), exhibit the largest mean diameters. The standard deviations are roughly within 15% of the mean, except for MM-6 which has a standard deviation of 3.0 nm. Through analysis of variance (ANOVA) with a significance level of $\alpha = 0.05$, there is a 95% chance that at least one of the means is statistically different. These findings suggest that there are composition-dependent effects that influence the growth rate of the synthesized nanoparticles, which impact

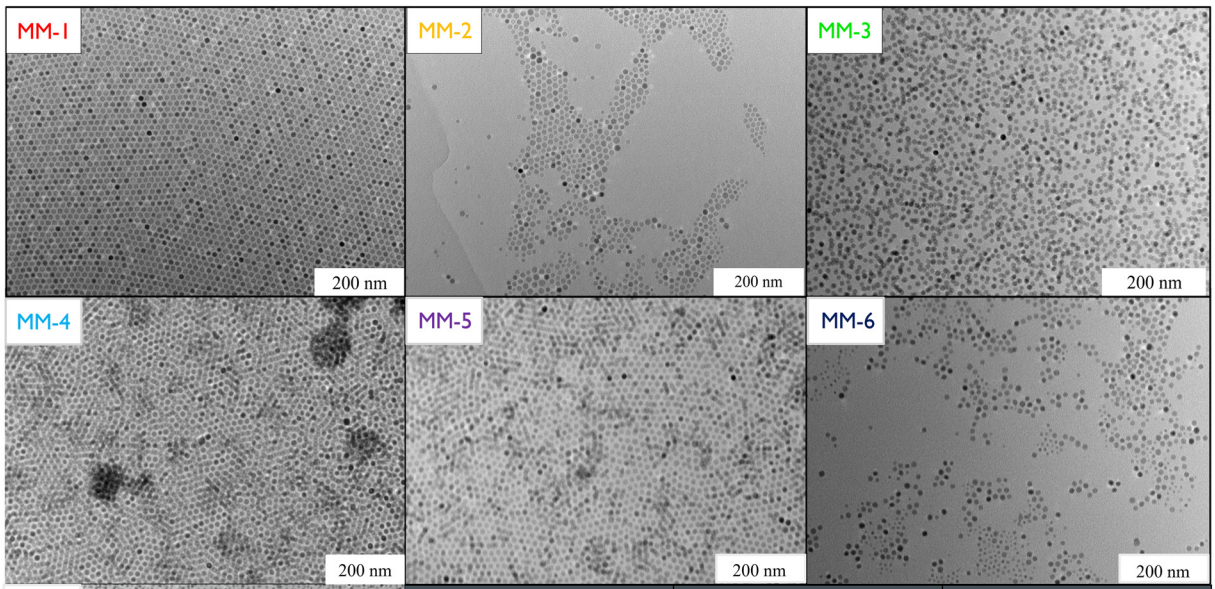

Sample	Mean Diameter [nm]	Standard Deviation
MM-1	10.4	1.0
MM-2	10.6	1.6
MM-3	10.5	1.3
MM-4	9.6	1.8
MM-5	10.0	1.6
MM-6	8.8	3.0
MM-7	8.4	1.1

Fig. 4 HR-TEM images of each mixed-cationic series, with the mean diameters and standard deviations given in the table in nm.

their mean diameters and homogeneity. Some discrepancy between targeted and synthesized compositions can be seen, highlighting the challenge of producing highly spherical, monodisperse nanoparticles while adjusting reagent ratios with different decomposition temperatures, and remain an area to be refined. Nonetheless, particles were produced in a manner with similar diameters allowing for the comparison of their resulting magnetic properties.

X-ray diffraction (XRD) data for the mixed-cationic nanoparticles have been included in the SI as shown in Fig. S1. Because the nanoparticle samples retained an oily layer after synthesis, the magnetic cores could not be separated completely, resulting in increased noise in the XRD spectra. Despite this, the spectra display evidence of peaks corresponding to the (311), (400), (511), and (440) planes, which are characteristic of the magnetite spinel ferrite structure (JCPDS card no. 85-1436). The oily layer also made energy-dispersive X-ray spectroscopy (EDS) impossible, as it was immediately carbonized upon contact with the electron beam, obscuring signals from the cations.

We also note that multiple oxidation states of manganese are possible and introduce complexity in determining the precise phase composition and cation distribution in the mixed-cationic nanoparticles. It is possible that a fraction of the reaction products formed magnetically dead, or weakly contributing phases that would not contribute to the magnetization response in the nanoparticles. Additional techniques, such as X-ray photoelectron spectroscopy (XPS) and Mössbauer spectroscopy are required to fully resolve the oxidation states of the cations in the nanoparticles and are a crucial direction for future work.

3.2 DC magnetometry

The effective anisotropy energy density is given by

$$K_{\text{eff}} = \frac{25 k_B T_B}{V_c}, \quad (3)$$

where k_B is Boltzmann's constant, T_B is the mean blocking temperature in K, and V_c is the volume of the nanoparticle in m^3. The mean blocking temperatures were calculated by finding the peak of the derivative of the (ZFC − FC) curves shown in Fig. 5A.[26,27] The mean blocking temperature (second column) and the mean DC K_{eff} (final column) inferred for each

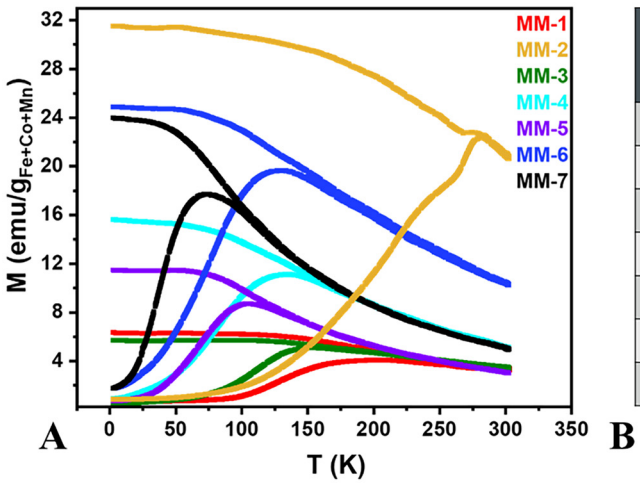

B

Sample	Mean Blocking Temperature T_B [K]	Target K_{eff} [J/m^3]	Mean DC K_{eff} [J/m^3]
MM-1	134	246,690	77,000
MM-2	204	340,000	130,000
MM-3	112	60,000	61,000
MM-4	85	63,000	57,000
MM-5	71	76,000	44,000
MM-6	78	14,000	55,000
MM-7	38	34,000	40,000

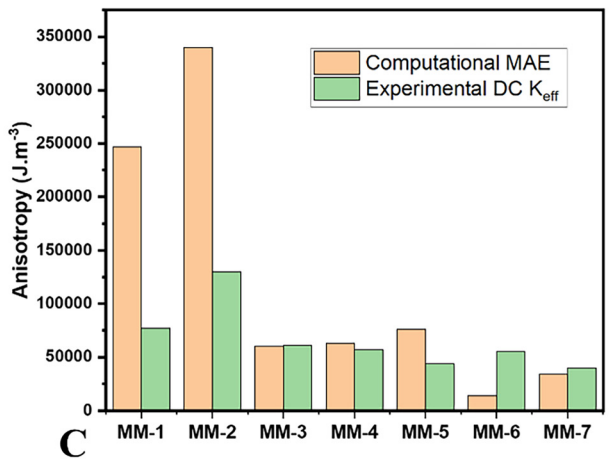

Fig. 5 (A) ZFC/FC curves for each nanoparticle series under an applied field of 100 Oe. (B) A table with mean blocking temperatures in K and DC K_{eff} values in J m^{-3}. (C) A bar graph comparing computational predictions of the MAE (orange colored) and K_{eff} values inferred from the DC measurements (green).

of the seven samples is displayed in Fig. 5B. To account for the nanoparticle size dispersion, a log–normal size distribution was constructed using the experimentally measured mean diameters and standard deviations from Fig. 4. DC K_{eff} was then calculated using the corresponding mean volumes from the log–normal distribution to reflect the size dispersion into the anisotropy values (Table S2) From Fig. 5B, MM-6 is shown to have a very high standard deviation (±3.0 nm) and is thus excluded from the compositional analysis of DC K_{eff}.

Analysis of the DC blocking temperatures for the mixed-cationic nanoparticle series show a compositional dependence and are compared in Fig. 5C, since the blocking temperature scales with the DC anisotropy energy density according to eqn (3). The high cobalt samples, (MM-1 and MM-2), are shown to have the highest mean blocking temperatures, (134 and 204 K). Their experimentally determined DC K_{eff} values (77 and 130 kJ m^{-3}, green bars in Fig. 5C) are significantly lower than the DFT predicted values (247 and 340 kJ m^{-3}, orange bars in Fig. 5C). MM-1 and MM-2 have the highest DC K_{eff} values out of all the samples, with MM-2 being the highest, corroborating the trend that is predicted by the DFT modeling.

The DC K_{eff} values for MM-3 to MM-7 are generally close to the predicted DFT values (Fig. 5C). MM-3, MM-4, and MM-7 are within 2–10% of their targeted values, showing high agreement. MM-5 is 42% lower than what was targeted. The results indicate that the low cobalt substituted spinel nanoparticles (MM-3 to MM-7), can be synthesized with predictable DC K_{eff} values, apart from MM-6, due to its larger size distribution. The results also show that generally, as the iron content increases and the manganese content decreases (MM-3 to MM-7), the K_{eff} values inferred from DC magnetometry generally decrease. In spinel ferrites, K_{eff} is comprised of magnetocrystalline anisotropy, surface anisotropy, and dipolar interactions which are heavily influenced by the type and distribution of cations in the tetrahedral and octahedral sites.[19] Increasing iron content while reducing manganese content shifts the multi-cationic nanoparticles to a more magnetite-like cation distribution, which is characterized by reduced lattice distortions and a lower single-ion anisotropy. It can also be seen that the predicted values for MM-3 to MM-5 increase slightly as manganese content decreases and then drop for MM-7, highlighting the sensitivity of the multi-cationic system to slight changes in composition and cation occupancy. As Co substitution is known to cause strong spin–orbit coupling, this increase in DC K_{eff} for the nanoparticles with higher cobalt content is expected, but was not as high as predicted.[28] It should be noted that in this mixed-cationic system, variations in cation occupancy between tetrahedral and octahedral sites, in addition to the multiple oxidation states of manganese, can lead to the formation of distinct magnetic sublattices with magnetically dead regions in the nanoparticles. These effects complicate the interpretation of the composition dependent shifts that were observed in the DC K_{eff} values. Additionally, small uncertainties in nanoparticle diameter or size dispersion can lead to large variations in the calculated DC K_{eff} values. DFT calculations also assume idealized, perfectly crystalline spinel lattices with fixed oxidation states and cation distributions, which will cause a discrepancy in K_{eff} when compared to synthesized nanoparticles. These difficulties underscore the importance of refining nanoparticle synthesis, structural characterization, and mathematical modeling.

3.3 Magnetic saturation analysis

The nanoparticles that were dispersed in the cotton balls were then placed in a PPMS to create magnetization *versus* field curves with a maximum DC magnetic field strength of 3 T, to experimentally determine the saturation magnetization (M_s) of each nanoparticle series. To convert emu g^{-1} to A m^{-1}, the density of the compositionally varied spinel nanoparticles was considered to be 5.18 g cm^{-3} which is roughly the density of magnetite.[29] The magnetization curves are shown in Fig. 6A, along with the resulting table of values for computationally and experimentally determined M_s in Fig. 6B.

As shown in Fig. 6C, the M_s values tend to experimentally increase (1.8–3.7 × 10^5 A m^{-1}, green bars) as manganese content decreases and as the iron content increases (MM-3 to MM-7). It has been shown that increasing iron content in single or bi-cationic spinel nanoparticles will increase M_s, which is in accordance with the experimental trend.[30,31] The DFT predicted M_s values do not follow this trend. MM-2 was experimentally determined to have the highest M_s (4.4 × 10^5 A m^{-1}) and MM-1 had a moderate M_s (2.6 × 10^5 A m^{-1}). The DFT predicted M_s values for MM-1 and MM-2 (5.9 × 10^5 and 5.6 × 10^5 A m^{-1}) also do not align with the experimentally determined data. The predicted values are all higher in magnitude for each mixed-cationic series ranging from 4.4–5.9 × 10^5 A m^{-1}. This disagreement between the experimental and computational values may arise from the non-ideal placement of the various cations in the nanoparticle's crystalline lattice during synthesis, as M_s depends on the net magnetic moment per formula unit determined by the difference between the moments of the tetrahedral and octahedral sites. The experimental increase in M_s with decreasing Mn content and increasing Fe content (MM-3 to MM-7) is likely due to more Fe^{3+} ions occupying octahedral sites, enhancing the magnetic moment per formula unit. The cation distribution in cobalt ferrite nanoparticles has been shown to alter M_s, with values decreasing with increasing cation inversion (Co^{2+} ions occupying tetrahedral sites and Fe^{3+} ions occupying octahedral sites).[32] For example, as MM-2 has less Mn content and higher Co and Fe content, fewer low-moment (Mn^{2+}) ions occupy the octahedral site but are present in the tetrahedral site, while higher moment ions (Fe^{3+} and Co^{2+}) occupy the octahedral site, maximizing the octahedral–tetrahedral moment difference in the lattice, leading to high M_s. Additionally, surface disorder effects are likely responsible for the consistently lower than predicted M_s values of the spinel nanoparticles, stemming from their smaller diameters of approximately 8.4–10.6 nm, an effect which has been reported for magnetite nanoparticles.[33] It is interesting to note that the inferred DC K_{eff} and the M_s values are decoupled, as increasing iron content (MM-3 to MM-7) generally decreases DC K_{eff}, but

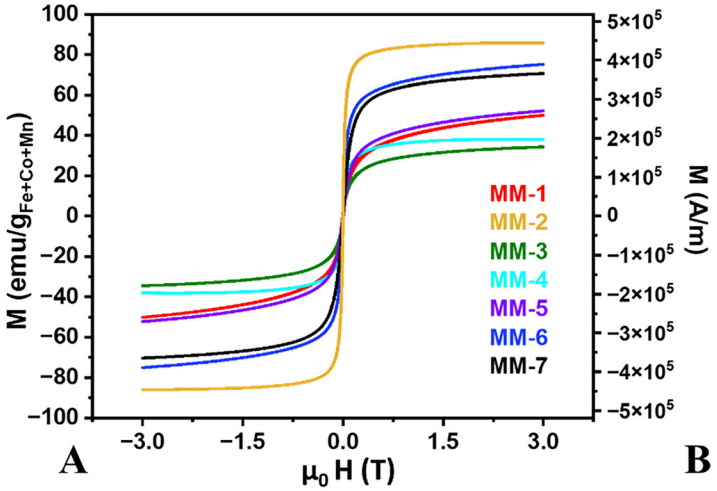

Sample	Computational M_s x 10^5 [A/m]	M_s x 10^5 [A/m]
MM-1	5.9	2.6
MM-2	5.6	4.4
MM-3	4.9	1.8
MM-4	5.0	2.0
MM-5	4.4	2.7
MM-6	5.2	3.8
MM-7	4.9	3.7

B

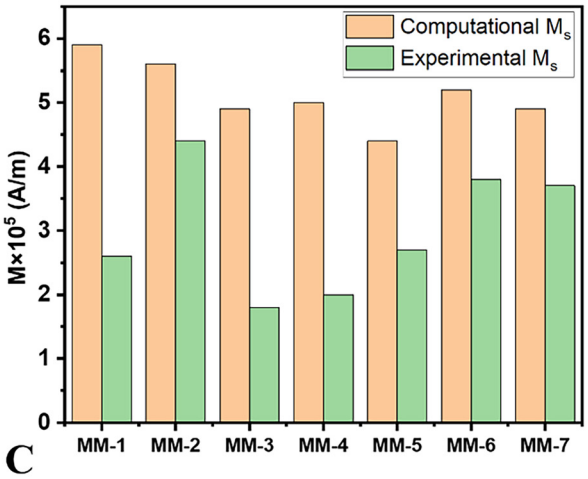

Fig. 6 (A) *M vs. H* curves for each mixed cation nanoparticle series with a maximum DC magnetic field strength of 3 T at 300 K. (B) Table and (C) bar graph depicting computationally predicted and experimentally determined M_s.

increases M_s. The possible presence of magnetically dead or weak regions would also contribute to decreasing overall M_s.

3.4 AC susceptibility analysis

AC susceptibility measurements allow one to probe the dynamics over magnetic anisotropy barriers because the peak in the imaginary component of the susceptibility is related directly to the magnetic relaxation time. The peak occurs when

$$\omega\tau = 1, \tag{4}$$

where ω is the AC field's angular frequency and τ is the relaxation time given in eqn (2). Debye showed this relation for dipoles that can physically rotate[34] and later it was shown *via* Landau Lifshitz Gilbert simulations that Néel–Arrhenius dynamics also follow this rule.[35] Changing the AC frequency shifts the susceptibility peak as a function of relaxation time or as a function of temperature, since the two are linked *via* eqn (2).

The AC magnetization data is shown in Fig. 7A for the MM-7 sample. The imaginary (out-of-phase) component of the AC susceptibility (χ'') was normalized to the real (in-phase) component of the AC susceptibility (χ') at 10 K and then plotted *versus* temperature. Higher field frequencies move the peak temperature higher since a lower relaxation time (faster) is needed to maintain the equality in eqn (4).

From these curves in Fig. 7A, the logarithm of the relaxation time $\ln(\tau) = \ln\left(\frac{1}{\omega}\right)$ was plotted as a function of peak temperature. This allows the Néel–Arrhenius (NA) – or Néel–Brown – eqn (2) to be fit to the data, which is shown in Fig. 7B. The best fit is obtained using a y-intercept corresponding to attempt time $\tau_0 = 1.3 \times 10^{-13}$ s and a slope proportional to the anisotropy energy density $K_{eff} = 63$ kJ m^{-3}. (Note that we use a mean magnetic volume for MM-7 $V_C = 3.3 \times 10^{-25}$ m^3, which is slightly larger than $\frac{4\pi\langle r\rangle^3}{3}$, with $\langle r\rangle$ the mean radius, because the distribution of volumes is skewed to higher values in a log–normal distribution.) The attempt time is quicker than what is usually assumed in DC measurements (0.001–1 ns) and the extracted anisotropy is roughly 50% larger than the

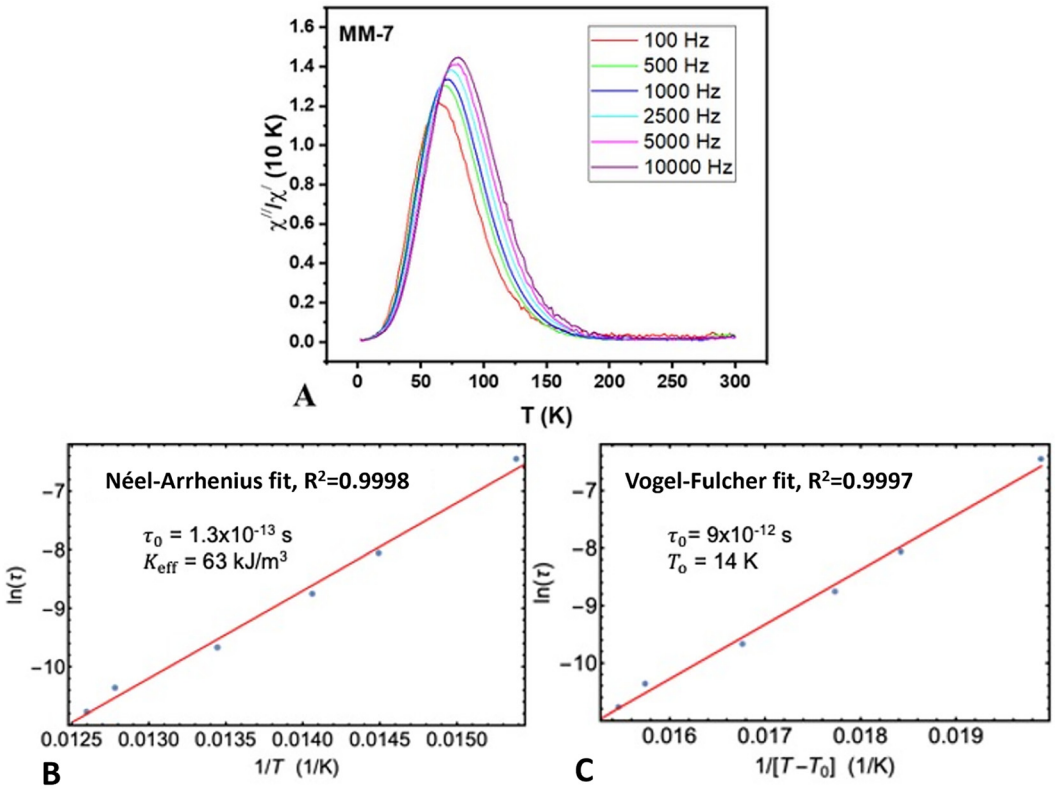

Fig. 7 (A) Representative AC susceptibility χ''/χ' *versus* temperature curves for MM-7, taken at frequencies ranging from 100 Hz to 10 000 Hz. The imaginary part of the magnetic susceptibility is normalized to the real part at 10 K. (B) The logarithm of the peak relaxation time ln(τ) *versus* inverse temperature 1/T with a NA fit through the data (eqn (2)). (C) The same data with a Vogel–Fulcher fit (eqn (5)) and with the anisotropy constrained to its DC value calculated from the mean diameter of the sample (K_{eff} = 40 kJ m^{-3}).

value extracted from DC measurements calculated from the overall mean (40 kJ m^{-3}).[36] R^2 values were computed using the inbuilt functions within Mathematica's NonlinearFindFit routine.[37] However, we note that the goodness of the fit (R^2 > 0.999) remains high no matter how we constrain the fit parameters. For example, constraining the anisotropy to be equal to the DC value calculated from the overall mean (K_{eff} = 40 kJ m^{-3}) results in a one-parameter fit with τ_0 = 0.25 ns and R^2 = 0.996, which also seems reasonable.

Table 1 shows the results of the unconstrained NA fit to the data, for all seven samples. One sees that the attempt times τ_0 (fourth column) are unphysically small, as noted by others.[38] The extracted anisotropy energy density K_{eff} values from the fit (third column) are also larger than the DC values in Fig. 5. However, the trend in the anisotropy is roughly the same with MM-2 having the largest value, followed by MM-1, and MM-7 having the lowest. This is encouraging.

Table 2 instead shows the same NA fit with the anisotropy constrained to the DC values (third column). Now the only fit parameter is the attempt time τ_0 in ns (fourth column). The

Table 1 The parameters K_{eff} and τ_0 extracted from a Néel–Arrhenius (NA) fit (eqn (2)) to the AC peak data from each sample. The R^2 value for each fit is given in the fifth column. The mean magnetic core volume is written in the second column for completeness

Sample	Mean V_c (10^{-25} m^3)	K_{eff} (kJ m^{-3}) from NA fit	τ_0 (s) from NA fit	R^2 of NA fit
MM-1	6.1	140	7.7×10^{-10}	0.9997
MM-2	6.7	415	3.6×10^{-26}	0.9993
MM-3	6.3	116	5.3×10^{-9}	0.9999
MM-4	5.1	94	1.4×10^{-6}	0.9995
MM-5	5.7	116	2.4×10^{-14}	0.9998
MM-6	4.9	94	4.7×10^{-6}	0.9997
MM-7	3.3	63	1.3×10^{-4}	0.9998

Table 2 The attempt time τ_0 extracted from a Néel–Arrhenius (NA) fit (eqn (2)) to the AC peak data from each sample, this time with the anisotropy constrained to the DC values calculated from the overall means. The R^2 value for each fit is given in the fifth column. The mean magnetic core volume is written in the second column for completeness

Sample	Mean V_c (10^{-25} m^3)	DC K_{eff} (kJ m^{-3})	τ_0 (ns) from NA fit	R^2 of NA fit
MM-1	6.1	77	0.35	0.995
MM-2	6.7	130	0.000015	0.996
MM-3	6.3	61	0.01	0.997
MM-4	5.1	57	0.03	0.995
MM-5	5.7	44	0.09	0.990
MM-6	4.9	55	0.10	0.995
MM-7	3.3	40	0.25	0.996

attempt time is reasonable for all samples apart from MM2 where it is a little small. The goodness of the fit is not as high as when the anisotropy is unconstrained (Table 1) but is still greater than 0.99 in all cases. Therefore, the different fits may only give qualitative information on the anisotropy barrier heights and attempt times.

Another option is to fit the AC data using the Vogel–Fulcher law,[39] namely

$$\tau = \tau_0 \exp\left[\frac{K_{\text{eff}} V_C}{k_B (T_B - T_0)}\right], \quad (5)$$

where the variables are defined in eqn (2), but with the addition here of a so-called interaction temperature T_0. Evidence of non-ideal behavior of the nanoparticles is noted due to the unphysically small τ_0 value obtained from the NA fitting. The Vogel–Fulcher model is assumed to be appropriate when there are weak interactions, which is likely the case for the multi-cationic nanoparticles, as they were dried into a fixed state for this experiment. Typically, this fit brings the attempt frequency to more reasonable numbers (for example, see ref. 38). As with the Néel–Arrhenius law, we found that a seemingly good fit ($R^2 > 0.999$) was obtained no matter how the parameters were constrained. For example, considering MM-7 again, constraining the anisotropy to the DC value (K_{eff} = 40 kJ m^{-3}) resulted in a fit with τ_0 = 0.009 ns, T_0 = 14 K, and R^2 = 0.9997, which are physically reasonable parameters. This fit is shown in Fig. 7C and is not considerably different from the NA fit shown in Fig. 7B. The AC susceptibility measurements measure the dynamics of the magnetic moments over the K_{eff} energy barrier. As Co^{2+} has strong spin–orbit coupling, an enhancement of the magnetocrystalline anisotropy energy is expected. MM-1 and MM-2 can be seen to have higher calculated K_{eff} values, which is reasonable as they have higher Co content compared to the other samples. Fe^{3+} has a larger magnetic moment than Co^{2+} but has a smaller spin–orbit contribution. Mn^{2+} has the weakest spin–orbit contribution. From Tables 1 & 2, the calculated K_{eff} values reflect the spin–orbit contributions of the cations that comprise the nanoparticles as they tend to decrease with increasing Fe content (MM-3 to MM-7). Again, it is interesting to note the decoupling between the nanoparticle's K_{eff} and M_s based on cationic composition. These interpretations must also be noted within the context of the sensitivity of the calculations to volume differences, and within the limitations of DFT modeling.

3.5 Specific absorption rate

The heating efficiencies of the nanoparticles were tested through calorimetric and AC SAR experiments. The masses of each of the nanoparticle series was taken by conserving the samples from each experiment and determining their elemental (cationic) content through ICP-OES. Each SAR is normalized with respect to the combined masses of Fe, Co, and Mn.

Most of the mixed-cationic series heated poorly at a field strength of 20 kA m^{-1} and frequencies near 205 kHz, as shown in Fig. 8. It has been shown that iron oxide nanoparticles that

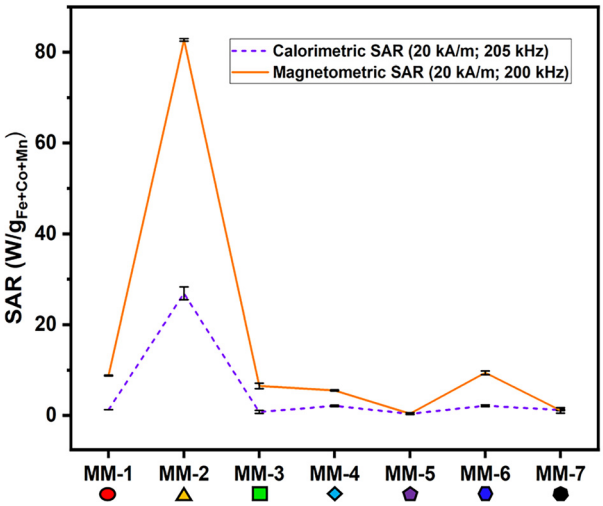

Fig. 8 Magnetometric SAR (solid line) for each mixed-cationic series at a field strength of 20 kA m^{-1} and a frequency of 200 kHz and calorimetric SAR (dashed line) for each mixed-cationic series at a field strength of 20 kA m^{-1}, and a frequency of 205 kHz.

are 10 nm in diameter are poor heaters, which match the results for many of the mixed-cationic series.[40] While the poor SAR values can arise from nanoparticle agglomeration, the toluene suspension likely limits significant clustering, suggesting that the low heating efficiency is primarily intrinsic to the nanoparticle size and composition. Notably, MM-2 displayed a much higher magnetometric and calorimetric SAR than the other nanoparticle series at these fields and frequencies. It has been shown that maximum heating for magnetic nanoparticles occurs at $\omega\tau \approx 1$, with ($\omega = 2\pi f$).[1,15] The Néel relaxation time corresponding to maximum heating at a given frequency f is given (similar to eqn (4)) by

$$\tau_{N_{\max}} = \frac{1}{2\pi f}. \quad (6)$$

For an AC field frequency of 200 kHz, the Néel relaxation for maximum heating is calculated to be 8 × 10^{-7} seconds, or 0.8 μs. The corresponding K_{eff} value for a magnetic nanoparticle of 10 nm in diameter to achieve this Néel relaxation time is 53 kJ m^{-3}, using eqn (2) and assuming τ_0 = 1 ns and T = 300 K. We note that this value is on the same order of magnitude as K_{eff} found from DC measurements (Fig. 5B) and AC measurements (Table 1) but there are too many approximations to claim that the nanoparticle composition with K_{eff} closest to this will heat the best. However, MM-2 exhibits by far the highest K_{eff} inferred from DC and AC measurements, and the highest heating, due to its higher K_{eff} from higher spin–orbit coupling from its increased Co content. In contrast, MM-3 to MM-7 have lower K_{eff} values due to their weaker spin–orbit coupling from their higher Mn and Fe content, producing Néel relaxation times that are too quick compared to the AC field timescales, causing their magnetic moments to closely follow the field, limiting their heat generation.

To understand this effect, the nanoparticles were subjected to higher magnetic field frequencies with results shown in Fig. 9. Due to instrumentational constraints, the highest possible frequency for the magnetometric SAR was chosen at 350 kHz. For the calorimetric SAR, the induction coil with the closest nominal frequency to this value (376 kHz), and highest field strength among these induction coils (12.7 kA m^{-1}) was used. The closest corresponding field strength setting (12 kA m^{-1}) was chosen for the magnetometric SAR. The magnetometric SAR values for MM-1 and MM-3 increased to 120 and 110 W g^{-1}, respectively, showing a large increase from the >10 W g^{-1} values at 200 kHz. The calorimetric SAR values also increased to 63 and 88 W g^{-1} from values below 1 W g^{-1}, as seen in Fig. 9. MM-2 also was determined to have an increase in AC SAR from 83 to 102 W g^{-1}, and an increase in calorimetric SAR from 26.9 to 85 W g^{-1}. MM-4 began to produce heat upon this frequency increase, measuring a calorimetric SAR value of 45 W g^{-1}, compared to its SAR of 2 W g^{-1} at 205 kHz. The rest of the mixed-cationic series did not produce heat at either magnetic field frequency, except for MM-7 measuring a calorimetric SAR of 25 W g^{-1} at the increased frequency.

At 376 kHz, the optimal Néel relaxation time is 4.2×10^{-7} seconds (0.42 μs), which is lower than that calculated earlier for 200 kHz The K_{eff} value that this would occur at is 47.6 kJ m^{-3} (again using eqn (2) and assuming τ_0 = 1 ns and T = 300 K). Increasing the AC field frequency would optimize heating for nanoparticles with a faster Néel relaxation time and a smaller K_{eff} than considered for 200 kHz. Therefore, while only MM-2 produced heat at 200 kHz, now other particle series produce heat as a smaller threshold K_{eff} value is required. This is seen as MM-1 through MM-4 produce heat, but the slightly smaller particles and those with lower K_{eff} values still do not. An increase in magnetocrystalline anisotropy with increasing cobalt content has been previously reported for 11 nm cobalt ferrite nanoparticles, which is attributed to higher spin–orbit coupling.[41] It was hypothesized that this increase in magnetocrystalline anisotropy tuned the Néel relaxation time around the driving frequency, which caused the enhancement of SAR with the increasing cobalt content of the nanoparticles. Néel relaxation time is highly sensitive to nanoparticle volume, which in turn will affect the optimal field and frequency for required for energy dissipation in addition to the influence of K_{eff}. While the nanoparticles in this study are relatively monodisperse and spherical, it should be noted that small variations in nanoparticle volume and additional contributions to K_{eff} such as dipolar interactions can influence the measured SAR. Despite these factors, it can be seen that altering cation composition can be used to tune K_{eff}, allowing for maximization of heating efficiency at specific alternating magnetic field frequencies.

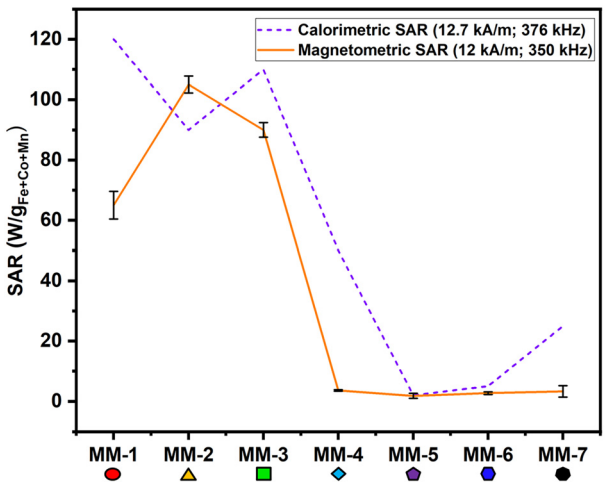

Fig. 9 Magnetometric SAR (solid line) for each mixed-cationic nanoparticle series at a field strength of 12 kA m^{-1} and a frequency of 350 kHz and calorimetric SAR (dashed line) for each mixed-cationic nanoparticle series at a field strength of 12.7 kA m^{-1}, and a frequency of 376 kHz.

4. Conclusions

In this work, DFT was used to guide the synthesis of seven nanoparticles series with controlled cationic compositions comprised of Fe, Co, and Mn that were roughly 10 nm in diameter. The actual compositions of the nanoparticles were verified by ICP-OES, and the size and shapes of the nanoparticles were verified by HRTEM. As the size and shape of the nanoparticles are relatively similar, the differences in K_{eff} and the resulting magnetic properties of the nanoparticles due to changes in their magnetocrystalline anisotropy were maximized.

The ZFC-FC curves illustrated differences in blocking temperatures with relative trends as predicted by DFT calculations, as their blocking peaks shifted to lower values as the iron concentration increased and the manganese concentration decreased for the nanoparticles, (MM-3 to MM-7), indicating a decrease in K_{eff} attributed to weaker spin–orbit coupling. It should be noted that the calculated DC K_{eff} values for the nanoparticles are highly sensitive to small changes in nanoparticle volume. The two spinel nanoparticles that were targeted towards higher K_{eff} values, (MM-1 and MM-2), displayed the highest blocking temperatures, indicating that they have a higher K_{eff}, verifying the DFT predictions. Their calculated K_{eff} values also followed this trend and were the highest of the series, with MM-1 having anisotropy energy density equal to 77 kJ m^{-3}, and MM-2 having 130 kJ m^{-3}, attributed to higher spin–orbit coupling.

The M_s of the nanoparticles also increased with increasing iron content, and decreasing manganese content, (MM-3 to MM-7), verifying the DFT calculations and coinciding with previously published results, illustrating that M_s can be targeted through altering K_{eff}. MM-1 had a lower M_s than predicted, and MM-2 had a higher M_s than predicted.

AC susceptibility data was generated for each sample, which were fitted to Néel–Arrhenius models. The fits gave rise to a wide range of inferred attempt time and anisotropy energy density values. However, the trend in the anisotropy strength

amongst the series of seven particles matched that extracted from the DC magnetometry data.

AC and calorimetric SAR experiments at a field strength of 20 kA m^{-1} and 200–205 kHz revealed that each mixed-cationic nanoparticle series heated poorly, except for MM-2. Increasing the calorimetric and AC field frequencies to approximately 376 and 350 kHz, respectively, revealed that the mixed-cationic nanoparticles with higher K_{eff} values, (MM-1 to MM-4), were able to generate heat, indicating that their higher K_{eff} values were able to slow down their Néel relaxation times into the optimal range for this AC magnetic field frequency. Therefore, altering K_{eff} through cationic composition can optimize the nanoparticles for specific AC magnetic field frequencies. These findings provide a predictive framework for designing optimized mixed-cationic nanoparticles for applications such as hyperthermia, catalysis, data storage, and nanoparticle imaging, where control over K_{eff} is paramount.

Author contributions

Alexander Malaj: writing – original draft, investigation, formal analysis, conceptualization, supervision. Cathryn Leies: investigation, formal analysis, data curation. Zachary Caprow: writing – review and editing, investigation, data curation. Venkata Rohit Punyapu: methodology, conceptualization, software. Ehimen A. Odion: investigation, data curation. Rachel Getman: methodology, conceptualization, writing – review and editing. Karen L. Livesey: writing – review and editing, formal analysis. Suvra Laha: writing – review and editing, investigation, supervision. O. Thompson Mefford: writing – review and editing, conceptualization, funding acquisition, project administration, resources.

Conflicts of interest

There are no conflicts to declare.

Data availability

Data for this article, including images, raw magnetic data, ICP concentrations, are available at Zenodo at https://doi.org/10.5281/zenodo.17517056.

Supplementary information (SI) is available. See DOI: https://doi.org/10.1039/d5nr04648c.

Acknowledgements

The authors would like to thank the National Science Foundation (CBET – 2146591), UnandUp Medical Technologies, and the Clemson Department of Materials Science and Engineering for their financial support. The authors would like to thank Dr Matthew Powell and Dr Brian Powell.

References

1 R. E. Rosensweig, *J. Magn. Magn. Mater.*, 2002, **252**, 370–374.
2 S. Dutz and R. Hergt, *Int. J. Hyperthermia*, 2013, **29**, 790–800.
3 I. Conde-Leboran, D. Baldomir, C. Martinez-Boubeta, O. Chubykalo-Fesenko, M. del Puerto Morales, G. Salas, D. Cabrera, J. Camarero, F. J. Teran and D. Serantes, *J. Phys. Chem. C*, 2015, **119**, 15698–15706.
4 H. Gavilán, S. K. Avugadda, T. Fernández-Cabada, N. Soni, M. Cassani, B. T. Mai, R. Chantrell and T. Pellegrino, *Chem. Soc. Rev.*, 2021, **50**, 11614–11667.
5 V. Russier, C. de-Montferrand, Y. Lalatonne and L. Motte, *J. Appl. Phys.*, 2013, **114**, 143904.
6 J. M. Coey, *Magnetism and magnetic materials*, Cambridge university press, 2010.
7 J. Birks, *Proc. Phys. Soc. B*, 1950, **63**, 65.
8 L. Bickford Jr, *Phys. Rev.*, 1950, **78**, 449.
9 S. Laurent, S. Dutz, U. O. Häfeli and M. Mahmoudi, *Adv. Colloid Interface Sci.*, 2011, **166**, 8–23.
10 E. Garaio, J. M. Collantes, J. A. Garcia, F. Plazaola, S. Mornet, F. Couillaud and O. Sandre, *J. Magn. Magn. Mater.*, 2014, **368**, 432–437.
11 J. W. Crawley, I. E. Gow, N. Lawes, I. Kowalec, L. Kabalan, C. R. A. Catlow, A. J. Logsdail, S. H. Taylor, N. F. Dummer and G. J. Hutchings, *Chem. Rev.*, 2022, **122**, 6795–6849.
12 V. R. Punyapu, J. Zhu, P. Meza-Morales, A. Chaluvadi, O. T. Mefford and R. B. Getman, *J. Magn. Magn. Mater.*, 2025, **621**, 172933.
13 A. J. Cohen, P. Mori-Sánchez and W. Yang, *Science*, 2008, **321**, 792–794.
14 E. Kiely, R. Zwane, R. Fox, A. M. Reilly and S. Guerin, *CrystEngComm*, 2021, **23**, 5697–5710.
15 J. Carrey, B. Mehdaoui and M. Respaud, *J. Appl. Phys.*, 2011, **109**, 083921.
16 M. N. Rahman and M. A. Hossain, *Mater. Today Sustain.*, 2026, **33**, 101252.
17 R. H. Kodama, *J. Magn. Magn. Mater.*, 1999, **200**, 359–372.
18 O. F. Odio, G. Tommasini, F. J. Teran, J. G. Ovejero, J. Rubín, M. Moros and S. Del Sol-Fernández, *Nanoscale Horiz.*, 2025, **10**, 2486–2503.
19 S. J. Salih and W. M. Mahmood, *Heliyon*, 2023, **9**(6), e16601.
20 N. Silvestri, H. Gavilán, P. Guardia, R. Brescia, S. Fernandes, A. C. S. Samia, F. J. Teran and T. Pellegrino, *Nanoscale*, 2021, **13**, 13665–13680.
21 F. C. Franyutti, S. A. Sabinas-Hernández, N. R. S. González, L. San Román-Escudero, E. Villalobos-Portillo, C. Marini, M. A. Méndez-Rojas and U. Salazar-Kuri, *Phys. B*, 2024, **687**, 416102.
22 A. Manohar, T. Suvarna, K. Chintagumpala, P. Manivasagan, E.-S. Jang, S. Sangaraju, B. A. Al-Asbahi and K. H. Kim, *Colloids Surf., A*, 2025, **708**, 136027.
23 B. D. Fellows, S. Sandler, J. Livingston, K. Fuller, L. Nwandu, S. Timmins, K. A. Lantz, M. Stefik and O. T. Mefford, *IEEE Magn. Lett.*, 2017, **9**, 1–5.
24 Z. Yan, S. FitzGerald, T. M. Crawford and O. T. Mefford, *JPhys Mater.*, 2021, **4**, 034013.

25 S. E. Sandler, B. Fellows and O. T. Mefford, *Anal. Chem.*, 2019, **91**, 14159–14169.
26 I. J. Bruvera, P. Mendoza Zélis, M. Pilar Calatayud, G. F. Goya and F. H. Sánchez, *J. Appl. Phys.*, 2015, **118**, 184304.
27 K. L. Livesey, S. Ruta, N. Anderson, D. Baldomir, R. W. Chantrell and D. Serantes, *Sci. Rep.*, 2018, **8**, 1–9.
28 M. Baričić, P. Maltoni, G. Barucca, N. Yaacoub, A. Omelyanchik, F. Canepa, R. Mathieu and D. Peddis, *Phys. Chem. Chem. Phys.*, 2024, **26**, 6325–6334.
29 S. Mi, R. Liu, Y. Li, Y. Xie and Z. Chen, *J. Magn. Magn. Mater.*, 2017, **428**, 235–238.
30 S. Kumar, G. W. Kim, B. Koo, S. Sharma, M. Knobel, H. Chung and C. G. Lee, *J. Nanosci. Nanotechnol.*, 2011, **11**, 555–559.
31 Y. Hadadian, H. Masoomi, A. Dinari, C. Ryu, S. Hwang, S. Kim, B. K. Cho, J. Y. Lee and J. Yoon, *ACS Omega*, 2022, **7**, 15996–16012.
32 A. Milutinović, Z.Ž Lazarević, M. Šuljagić and L. Andjelković, *Metals*, 2024, **14**, 833.
33 G. F. Goya, T. Berquo, F. C. Fonseca and M. Morales, *J. Appl. Phys.*, 2003, **94**, 3520–3528.
34 P. J. W. Debye, *Polar molecules*, Chemical Catalog Co., New York, 1929.
35 J. L. García-Palacios and F. J. Lázaro, *Phys. Rev. B: Condens. Matter Mater. Phys.*, 1998, **58**, 14937–14958.
36 J. Leliaert, A. Coene, G. Crevecoeur, A. Vansteenkiste, D. Eberbeck, F. Wiekhorst, B. Van Waeyenberge and L. Dupré, *J. Appl. Phys.*, 2014, **116**, 163914.
37 W. Research, Wolfram Language Documentation, https://reference.wolfram.com/language/tutorial/NumericalOperationsOnData.html#382930361.
38 B. Aslibeiki, P. Kameli, H. Salamati, M. Eshraghi and T. Tahmasebi, *J. Magn. Magn. Mater.*, 2010, **322**, 2929–2934.
39 S. Shtrikman and E. Wohlfarth, *Phys. Lett. A*, 1981, **85**, 467–470.
40 S. Tong, C. A. Quinto, L. Zhang, P. Mohindra and G. Bao, *ACS Nano*, 2017, **11**, 6808–6816.
41 J. Mohapatra, M. Xing and J. P. Liu, *AIP Adv.*, 2018, **8**, 056725.